applied sciences

MDPI

Article

Time-Lapse Electrical Resistivity Tomography for Seepage Failure Monitoring in Earth-Rock Dams

Lei Tan [1,2,3], Binyang Sun [1,*] and Pingsong Zhang [1]

1 School of Earth and Environment, Anhui University of Science and Technology, Huainan 232001, China; ltan126@126.com (L.T.); pszhang1971@163.com (P.Z.)
2 Zhejiang Institute of Hydraulics & Estuary (Zhejiang Institute of Marine Planning and Design), Hangzhou 310020, China
3 Zhejiang Guangchuan Engineering Consulting Co., Ltd., Hangzhou 310020, China
* Correspondence: bysun_1993@163.com

Abstract

Seepage failure is a primary cause of reservoir dam breaches. Conventional monitoring cannot reveal leakage paths across the dam, and static surveys miss weak-zone evolution. To address these challenges, this study constructs a typical geoelectric numerical model of low-resistivity expansion at a dam abutment. It systematically analyzes the response characteristics of apparent resistivity, independently inverted resistivity, and time-lapse resistivity imaging to the seepage failure process and validates the method through physical model tests and field observations. Inverted resistivity delineates hazards better than apparent resistivity, especially for small targets. Using the initial non-leakage model as a baseline, the resistivity-change profile obtained by ratio processing reveals the development trend of the hazard. Time-lapse inversion suppresses spurious artifacts from independent inversions and images the gradual expansion of the seepage weak zone. The L1-norm-constrained differential inversion further improves the convergence of the low-resistivity region and the accuracy of the anomaly center. Physical tests show rising water level reduces resistivity, especially in leakage-prone areas. Field tests show that after grouting, deep resistivity increases while shallow resistivity decreases. The results demonstrate that the time-lapse differential inversion algorithm based on the L1 norm accurately captures the spatiotemporal evolution of leakage hazards in earth-rock dams, providing reliable technical support for reservoir safety monitoring and evaluation.

Keywords: earth-rock dam leakage; time-lapse resistivity; L1 norm; differential inversion; dynamic monitoring

Academic Editor: Nikolaos Koukouzas

Received: 27 April 2026
Revised: 27 May 2026
Accepted: 3 June 2026
Published: 4 June 2026

1. Introduction

Seepage failure is a critical threat to earth-rock dams, often causing reservoir breaches [1]. With climate change, extreme rainfall has become more frequent, challenging dam safety margins [2]. Conventional monitoring uses boreholes and point sensors, giving only local water levels and missing the overall seepage field. Most leakage occurs at dam–abutment or dam–culvert interfaces, creating monitoring blind spots [3,4]. Full-section, time-varying seepage monitoring is urgently needed.

Electrical Resistivity Tomography (ERT) offers wide coverage and sensitivity to water-induced resistivity changes [5]. ERT has proven effective for dam leakage detection [6,7]. For example, ref. [5] combined resistivity and induced polarization to evaluate embankment stability; [6] used mise-à-la-masse and tracer tests to map karst conduits; [7] studied pseudo-flow field sensitivity for leakage inlet positioning. Newer methods include passive infrared thermography, self-potential, towed cable arrays, magnetic sensors, and fiber-optic sensing. Despite advances, most ERT surveys are static, unable to track seepage or give early warning [8,9].

Time-lapse ERT uses fixed electrodes to monitor resistivity changes, suppressing errors and improving sensitivity [10–12]. Applications include embankment seepage detection and long-term dam safety assessment [13–15]. Recent advances have integrated time-lapse ERT with IoT and 5G technologies, enabling real-time data acquisition and automated inversion for dynamic monitoring of dam leakage [16].

Processing time-lapse ERT data remains challenging. Several inversion strategies exist (independent, differential, ratio, cascaded, time-constrained) [17–21]. The choice of regularization norm—L2 (smooth) vs. L1 (sharp boundaries)—affects the resolution of growing seepage zones [21]. The L2-norm regularization tends to produce smooth resistivity models, which may smear sharp boundaries of localized seepage zones. In contrast, the L1-norm regularization promotes piecewise-constant models with sharp edges, making it more suitable for delineating the boundaries of a growing leakage anomaly [22]. Recent studies have also advanced full-gradient difference inversion schemes for time-lapse ERT data, further enhancing detection of subtle temporal resistivity changes [23]. Therefore, we compare both norms in this study and adopt the L1-norm constrained difference inversion as the preferred method.

A previous study by the same research group (Tan et al., 2026) [24] investigated the Fengtongwu Dam using time-lapse ERT, focusing on electrode array comparison and remote electrode placement. The present work extends that study by: (i) systematically comparing independent inversion, ratio imaging, and difference inversion for tracking progressive weak-zone expansion; (ii) demonstrating the superiority of L1-norm regularization in artifact suppression and boundary delineation; (iii) validating the numerical findings with a scaled physical model. Furthermore, an independent geophysical investigation by Guo et al. (2022) [25] using self-potential (SP) and ERT on the same dam identified three major seepage pathways in the left abutment, spatially coinciding with the high-grout-consumption zones in our grouting design, providing strong multi-method validation.

The objective of this study is to systematically evaluate different time-lapse resistivity processing methods for monitoring the spatiotemporal evolution of seepage weak zones in earth-rock dams and to identify the optimal inversion strategy. The specific goals are three-fold: (1) compare the sensitivity of apparent resistivity, independent inversion, ratio imaging, and L2-/L1-norm time-lapse difference inversion to small and progressively expanding leakage targets; (2) identify the most reliable method that eliminates the "sensitivity jump" and artifacts; (3) validate the selected method through a physical model test and an engineering case study. To achieve these goals, we first construct a geoelectrical model of an abutment leakage zone with progressive expansion for numerical simulation (Section 3). Next, we conduct a scaled physical model test (Section 4). Finally, we apply the method to a real engineering case (Section 5). All measurements employ the Wenner pole-dipole array.

2. Time-Lapse Electrical Resistivity Tomography Method

2.1. Basic Principles

ERT injects current via electrodes and measures potential differences to calculate apparent resistivity. Leakage zones have increased water content and conductivity, leading

https://doi.org/10.3390/app16115654

to lower resistivity. In a homogeneous half-space, the potential $U(x, y, z)$ from a point source satisfies the Laplace equation:

$$\nabla \cdot \left(\frac{1}{\rho(x,y,z)} \nabla U(x,y,z) \right) = -2I\delta(x-x_0)\delta(y-y_0)\delta(z-z_0) \tag{1}$$

Equation (1) is the governing equation for the electric potential from a point current source in a homogeneous half-space. Apparent resistivity ρ_s is given by:

$$\rho_s = K\frac{\Delta U}{I} \tag{2}$$

where K is the geometric factor depending on electrode positions. The electrode positions directly affect the depth of investigation and lateral resolution via K. The essence of time-lapse ERT is the introduction of the time dimension: by repeating measurements with fixed electrode positions and comparing resistivity changes over time, time-invariant geological noise is suppressed, and leakage-induced anomalies are highlighted. Time-lapse ERT adds a time dimension, i.e., the resistivity becomes a function of space and time, $\rho(x, y, z, t)$. Equation (1) represents the static case where time is constant.

Forward modeling was performed using the finite element method to solve Equation (1), with Dirichlet boundary conditions (zero potential at the boundaries of the computational domain). The resulting linear systems were solved iteratively using the conjugate gradient solver to reduce memory requirements and improve computational efficiency. The survey line consisted of 64 electrodes with 1 m spacing, using the Wenner pole-dipole array (one current electrode A on the line, the distant current electrode B placed far away perpendicular to the line, and potential electrodes M, N on the same side as A). This array is sensitive to vertical resistivity contrasts such as those found in dam–abutment contact zones and offers a high signal-to-noise ratio and focused anomaly response. To simulate field noise, 3% Gaussian random noise was added to the synthetic data. The forward mesh was locally refined near electrodes and anomaly boundaries, with a maximum element size of 0.5 m. Based on field experience, typical noise levels in ERT surveys of earth-rock dams range between 2% and 5% [26]. The chosen survey parameters (64 electrodes, 1 m spacing, Wenner pole-dipole array) provide a balance between spatial resolution and depth of investigation. For the dam geometry (height 15 m, abutment slope 31°), the 1 m spacing yields a horizontal resolution of approximately 1–2 m in the shallow zone (0–5 m depth) and 3–5 m at greater depths, which is sufficient to resolve the expected dimensions of the seepage weak zone (horizontal extent 5–13 m).

2.2. Time-Lapse Differential InversionTime-Lapse Differential Inversion Method

The ERT inverse problem is nonlinear and ill-posed. The forward problem can be written as:

$$d = g(m) \tag{3}$$

where d is the observed data vector, and m is the model parameter vector (resistivity distribution). The forward operator g solves Equation (1) for a given resistivity model and computes the predicted apparent resistivities for all four-electrode combinations used in the survey.

At baseline time t_0 and monitoring time t_1:

$$d_0 = g(\mathrm{m}_0) + \varepsilon_s + \varepsilon_0,\ d_1 = g(\mathrm{m}_1) + \varepsilon_s + \varepsilon_1 \tag{4}$$

where ε_s is systematic error and ε_0, ε_1 are random noise. Subtracting removes ε_s:

$$\Delta d = d_1 - d_0 \approx g(m_1) - g(m_0) + (\varepsilon_1 - \varepsilon_0) \tag{5}$$

The independent Occam inversion minimizes to:

$$\Phi = \|W_{\mathrm{d}}(\mathrm{d} - \mathrm{g}(\mathrm{m}))\|^2 + \alpha\|R\mathrm{m}\|^2 \tag{6}$$

where W_{d} is the data weight matrix, R is the roughness matrix, and α is the smoothing parameter. The L2-norm yields smooth models; the L1-norm promotes sharp boundaries, advantageous for delineating leakage edges [27].

For difference inversion, the objective function becomes:

$$\Phi_{\mathrm{diff}} = \|W_{\mathrm{d}}[(\mathrm{d}_1 - \mathrm{d}_0) - (\mathrm{g}(\mathrm{m}_1) - \mathrm{g}(\mathrm{m}_0))]\|^2 + \alpha\|\mathrm{R}(\mathrm{m}_1 - \mathrm{m}_0)\|^2 \tag{7}$$

where m_0 is the baseline model. This formulation directly regularizes the model change relative to the background, further suppressing time-invariant artifacts.

In practice, the inversion handles noise by incorporating the data weight matrix Wd, which is set inversely proportional to the estimated standard deviation of each measurement. For independent inversion (Equation (6)), the L2-norm produces smoothly varying resistivity models, while the L1-norm promotes sharp transitions. For time-lapse monitoring, difference inversion (Equation (7)) directly inverts the change in data Δd relative to a baseline, using the baseline model m_0 as a reference. This approach suppresses time-invariant artifacts (e.g., static shifts due to electrode positioning) and is less sensitive to noise than independent inversion of each time step followed by subtraction. Recent advances in time-lapse ERT inversion have introduced full-gradient difference inversion schemes that optimize both spatial and temporal roughness simultaneously [23]; while our approach uses a sequential difference inversion, the full-gradient scheme represents a promising direction for future improvement.

2.3. Establishment of the Initial Non-Leakage Baseline Model

The initial non-leakage model represents the background electrical field under the "healthy" condition of the dam. It was established through the following steps: (1) collect geological survey data and construction records to determine the resistivity ranges of the normal dam body, abutment, and bedrock; (2) conduct a complete ERT background survey during the period of lowest reservoir water level and without any visible leakage (in numerical simulation and physical model, the initial state with no imposed leakage condition is used); (3) use the resistivity distribution obtained from inverting the background data as the baseline model. This model serves as the denominator for ratio images and the reference model m_0 in the difference inversion objective function, maximally eliminating time-invariant errors and improving detection sensitivity for the seepage weak zone.

2.4. Flowchart of Forward and Inversion Process

Figure 1 illustrates the complete workflow of forward modeling, iterative inversion, and post-processing evaluation. The workflow is divided into three stages.

Stage 1 (Forward modeling): Synthetic apparent resistivity data are generated based on model components (electrode array type, spacing, geometry; current source intensity and contact resistance; observation system configuration), geoelectric parameters (dam structure, anomaly zone geometry and boundary type, resistivity model subdivision and random noise), and numerical settings (FEM solver with Dirichlet boundary conditions, mesh refinement, data filtering).

Stage 2 (Resistivity inversion—iterative process): Inversion settings include stop criteria (maximum iterations, target RMS, error reduction), initial model (pseudosection or average apparent resistivity), and regularization (L1-norm or L2-norm). Two inversion strategies are available: independent inversion and time-lapse difference inversion. The core inversion follows an iterative loop: the initial model m_0 is used for forward calculation to obtain d_{calc}. The synthetic data are compared with observed data d_{obs} to compute the error Δd. If convergence criteria are not met, the model is updated using the L1-norm or L2-norm objective functions, and the loop returns to forward calculation.

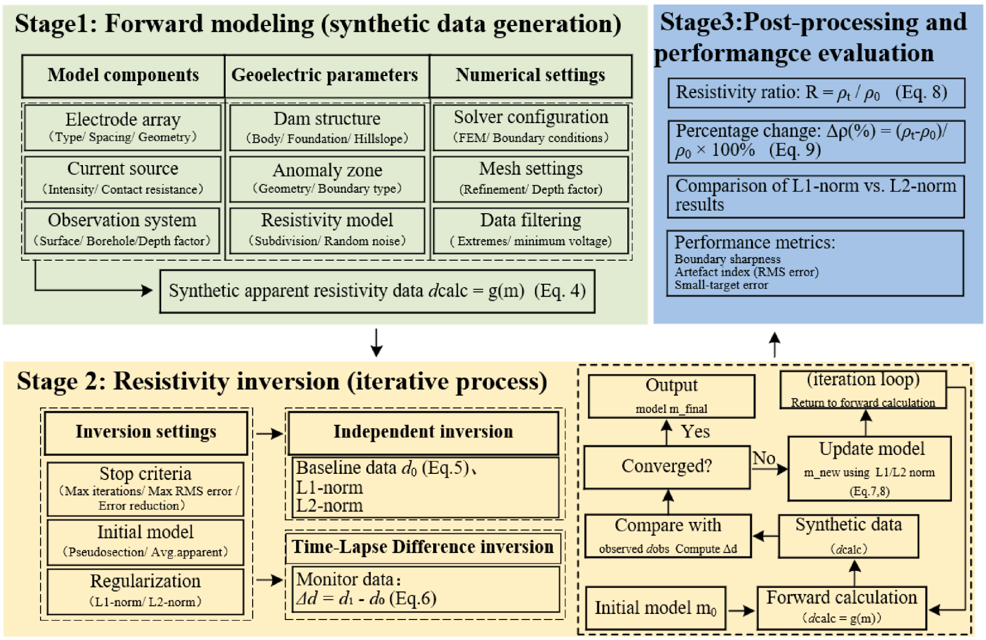

Figure 1. Comprehensive workflow of forward modeling, iterative inversion, and post-processing evaluation.

Stage 3 (Post-processing and performance evaluation): The resistivity ratio and percentage change are calculated. L1-norm and L2-norm results are compared, and inversion quality is assessed using performance metrics such as boundary sharpness, RMS artifact index, and small-target error.

3. Simulation Analysis

3.1. Theoretical Model

Figure 2 shows the geoelectric model of a left abutment leakage hazard. The model is a 2D rectangular profile of length 63 m and height 20 m, consisting of bedrock, a normal dam body, and a seepage weak zone. The bedrock (resistivity 1000 Ω·m) is distributed in both abutment slopes and the foundation. The two abutment slopes are symmetric about the dam centerline with a dip angle of 31°; their crests are 1.5 m below the dam crest, and the bedrock foundation thickness is 5 m. The normal dam body (resistivity 200 Ω·m) fills the area between the slopes. The seepage weak zone (resistivity 20 Ω·m) is located at the left abutment and expands progressively from (a) to (e):

(a) Stage a (smallest): Right-triangular shape. Its left edge is 11.7 m from the left dam end, its top is 7.8 m below the dam crest, with a horizontal extent of 5.3 m and a vertical extent of 2.9 m.
(b) Stage b: Expanded from Stage a by 2 m horizontally to the right and 1 m vertically upward.
(c) Stage c: Expanded from Stage b by another 2 m horizontally and 1 m vertically (total: +4 m horizontal, +2 m vertical relative to Stage a).
(d) Stage d: Expanded from Stage c by another 2 m horizontally and 1 m vertically (total: +6 m horizontal, +3 m vertical).
(e) Stage e (largest): Expanded from Stage d by another 2 m horizontally and 1 m vertically (total: +8 m horizontal, +4 m vertical).

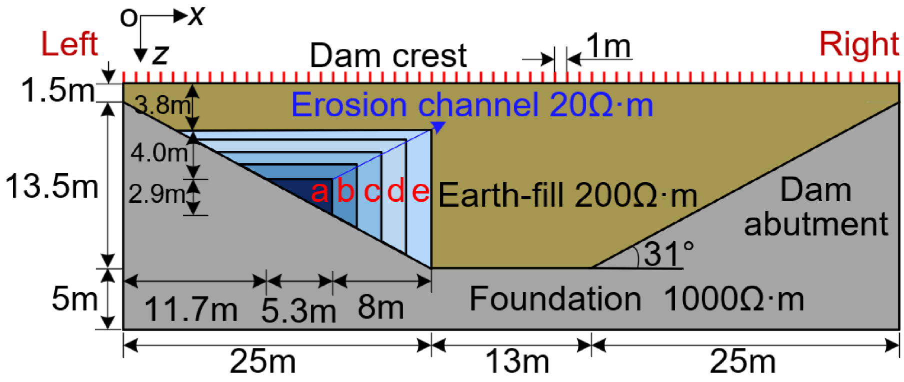

Figure 2. Geoelectric model of an earth-rock dam showing progressive expansion of the seepage weak zone (a → e) at the left abutment.

Black solid boxes indicate the weak-zone location. This model is used to evaluate the response of time-lapse resistivity imaging to seepage targets of different sizes.

3.2. Independent Inversion Analysis

Using the Wenner pole-dipole array with 3% noise, each expansion stage was modeled. The apparent resistivity sections (Figure 3, left column) were directly plotted without inversion. For the background model (Figure 3a, left column), the apparent resistivity section is asymmetric because the Wenner pole-dipole array is more sensitive to left-side anomalies. This background section corresponds to the no-leakage case. When the weak zone is present at Stage a (small size, Figure 3b, left column), the apparent resistivity section shows no clear low-resistivity anomaly, as the perturbation from such a small target is below the noise level. When the weak zone expands to Stage b (Figure 3c, left column), the high-resistivity area on the left gradually shrinks, but no closed low-resistivity contour appears. At Stage c (Figure 3d, left column), an elliptical low-resistivity anomaly with a long horizontal axis becomes visible, but its position is shifted relative to the true location. At Stages d and e (Figure 3e,f, left column), the anomaly is larger than the actual weak zone due to the volume effect.

Inverted resistivity sections (Figure 3, right column) better represent the background structure. The left and right bank slopes are clearly visible, and the overall resistivity distribution is more consistent with the true model. In Figure 3b (right column, Stage a), the inverted section exhibits a slight distortion of the abutment contour near the weak-zone location. In Figure 3c (right column, Stage b), a closed low-resistivity body appears in the inverted section at a horizontal position of approximately 20 m. For Stages c–e (Figure 3d–f, right column), inverted sections show an expanding low-resistivity zone with values near 20–50 Ω·m. However, the shape of the anomaly is somewhat smoother than the true sharp triangle, and the boundaries are not sharply defined.

Sensitivity jumps: the anomaly is barely detectable at Stage a, becomes visible at Stages b–c, then growth slows at Stages d–e. This nonlinear behavior is problematic for early warning because it implies that the method may miss a small leak and then suddenly show a large anomaly when the leak has already become significant.

The normalized ratio image is defined as:

$$R = \frac{\rho_t}{\rho_0} \tag{8}$$

where ρ_t is the resistivity at the monitoring time, and ρ_0 is the baseline (no-leakage) model resistivity. Ratio processing enhances relative changes and highlights low-resistivity anomalies caused by seepage, but it can also amplify noise and inversion artifacts, especially in areas where the background resistivity is low or shows little variation. Therefore, ratio images should be interpreted together with the original inversion results [28]. The resulting ratio images are shown in Figure 4.

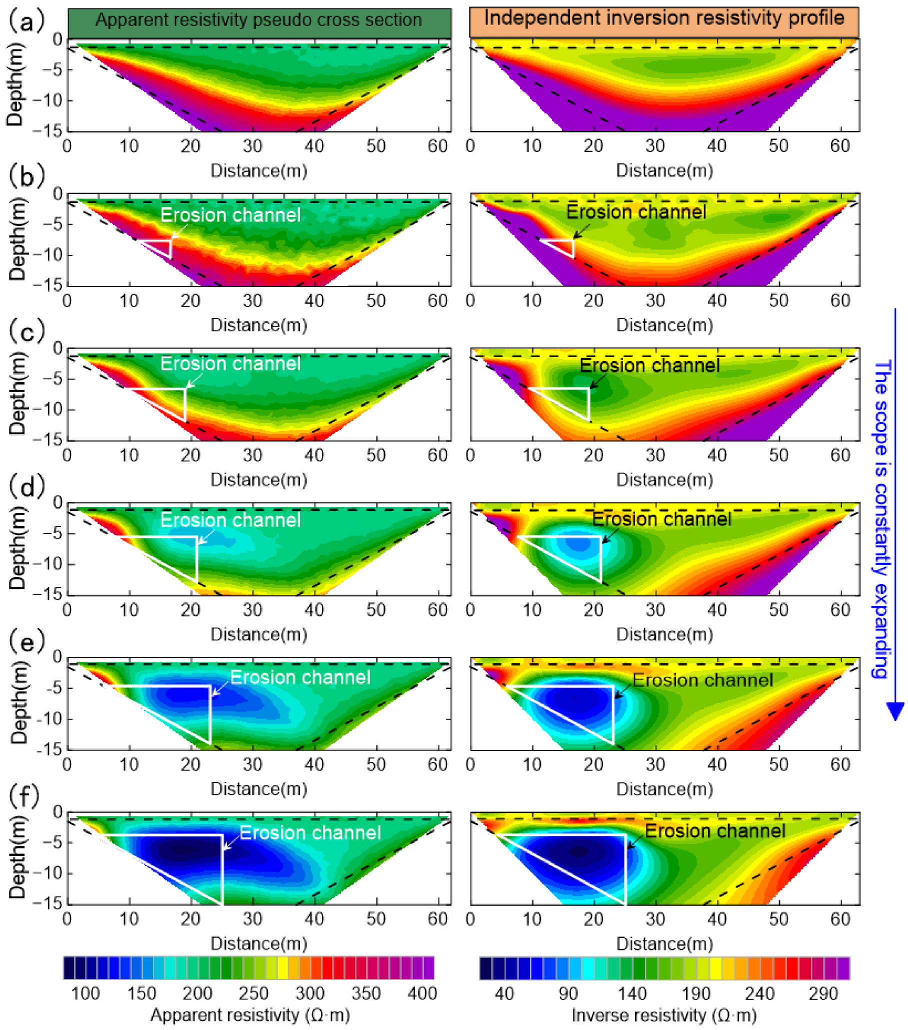

Figure 3. Independent inversion results (L2-norm) at different stages of weak-zone expansion. Left column: apparent resistivity sections; right column: inverted resistivity sections. Stages correspond to models in Figure 2: (**a**) Background (no leakage), (**b**) Stage a (smallest weak zone), (**c**) Stage b, (**d**) Stage c, (**e**) Stage d, (**f**) Stage e (largest). White dashed circles indicate the true weak-zone location. 3% Gaussian noise added. Inversion parameters: max iterations = 8, target RMS = 2, smoothing factor = 100, damping factor = 100. Final RMS errors: (**a**) 1.60%, (**b**) 1.63%, (**c**) 1.75%, (**d**) 1.97%, (**e**) 1.61%, (**f**) 1.75%.

The apparent resistivity ratio shows a gradual decrease in the left abutment as the weak zone expands, but the anomaly is diffuse and poorly defined at Stage a. The inverted resistivity ratio (bottom row) provides clearer images: at Stage a, a small area of reduced resistivity appears at the correct location; at Stages b and c, the low-ratio zone becomes more distinct and shows a closed contour; at Stages d and e, the low-ratio zone expands further. Spurious anomalies appear on the right bank from inversion errors in the ratio calculation. Ratio processing improves early detection but retains artifacts and the jump phenomenon.

3.3. Time-Lapse Differential Inversion for Numerical Simulation

In the numerical simulation, we defined five discrete monitoring time points corresponding to Stages a to e of weak-zone expansion. Forward data were generated independently for each stage, and 3% noise was added. The time-lapse difference inversion used the data from before Stage a (i.e., the background model) as the baseline and then performed difference processing for Stages a–e individually. Figure 5 shows the percentage change in resistivity obtained by time-lapse differential inversion using L2 and L1 norm constraints.

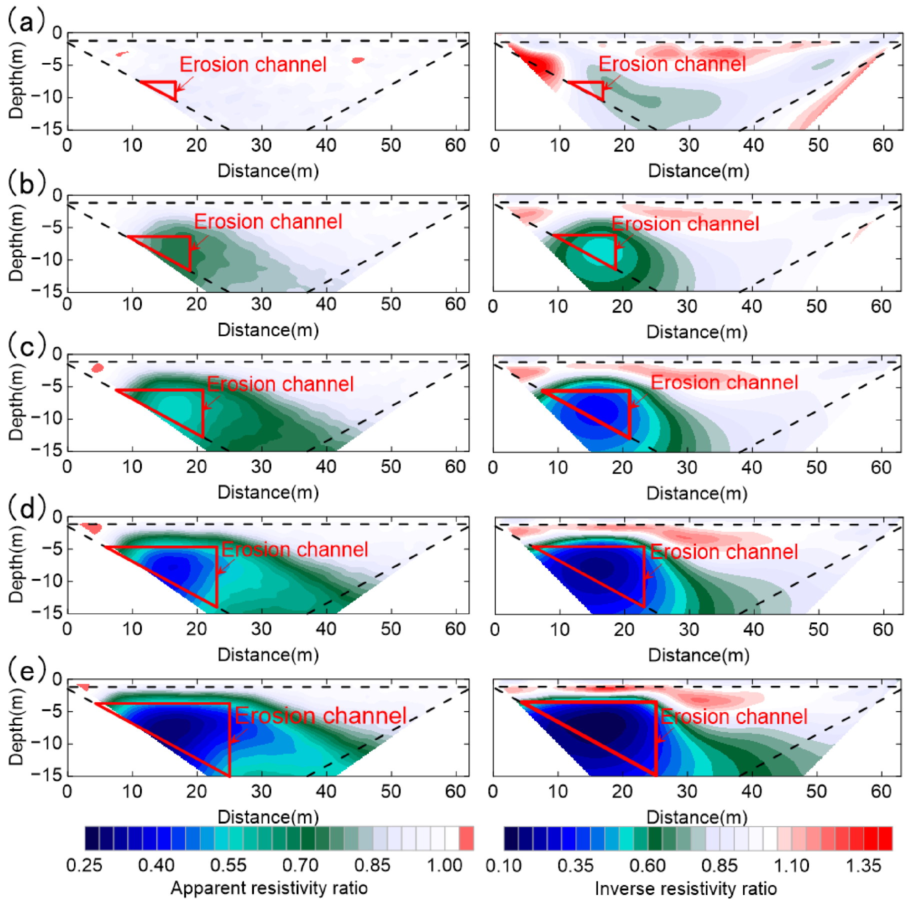

Figure 4. Resistivity ratio (relative to the baseline no-leakage model). Left column: apparent resistivity ratio; right column: inverted resistivity ratio. (**a**) Stage a, (**b**) Stage b, (**c**) Stage c, (**d**) Stage d, (**e**) Stage e.

The percentage change in resistivity is defined as:

$$\Delta\rho(\%) = \frac{\rho_t - \rho_0}{\rho_0} \times 100\% \tag{9}$$

where ρ_0 is the initial or baseline resistivity and ρ_t is the resistivity from a subsequent monitoring survey. Negative values indicate a resistivity decrease (increased water saturation), and positive values indicate a resistivity increase (drying or solidification).

L2-norm results (Figure 5, left column) identify the weak zone at Stage a, improving on independent inversion. The anomaly appears as a closed low-percentage region (blue) at the correct location. As the weak zone expands to Stages b and c, the low-percentage region expands accordingly, and the percentage decrease becomes larger (from about –10% at Stage a to –30% at Stage c). L2-norm results show background artifacts—small changes far from the anomaly, especially near the right bank and at depth. These artifacts typically have magnitudes below 15%, but they could be misinterpreted as real changes in a field setting.

L1-norm results (Figure 5, right column) are superior. At Stage a, the anomaly is sharply defined and matches the true triangular geometry, with its left boundary aligned to the abutment contact. As the weak zone expands to Stages b and c, the anomaly remains compact, and the percentage decrease increases progressively. At Stages d and e, the low-resistivity region expands, but the anomaly core remains centered at the original leakage location. L1-norm inversion delineates the expanding zone and highlights the persistent leak source. Background artifacts are suppressed; only minor, local artifacts remain.

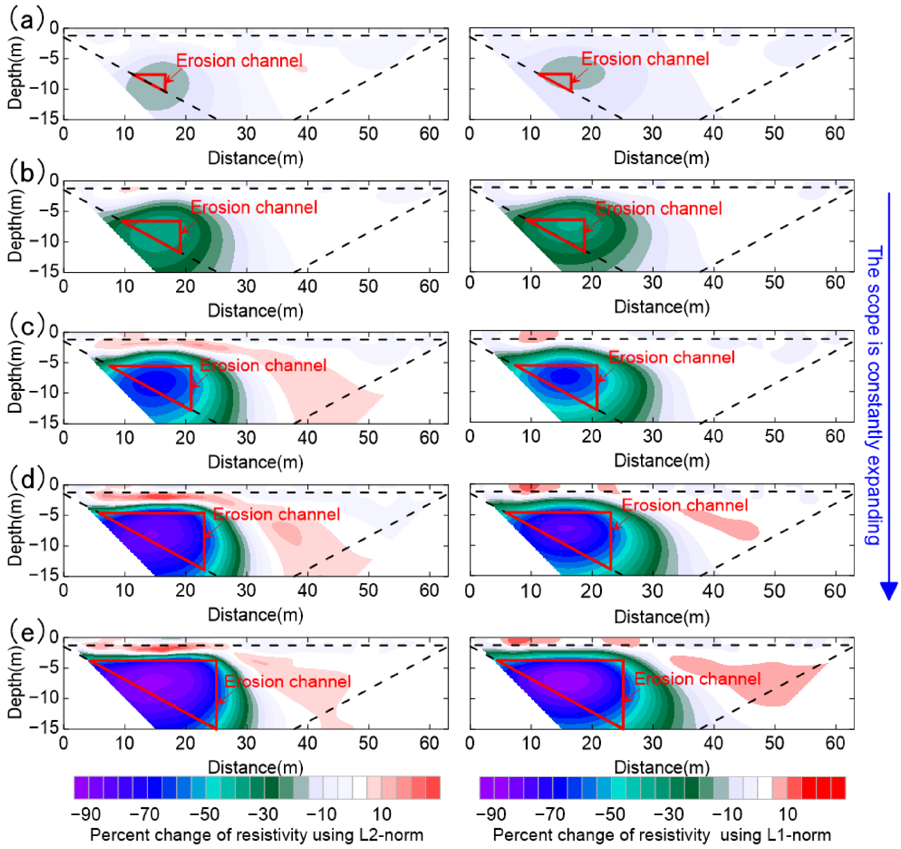

Figure 5. Time-lapse resistivity percentage change obtained by differential inversion. Left column: L2-norm constraint; right column: L1-norm constraint. (**a**) Stage a, (**b**) Stage b, (**c**) Stage c, (**d**) Stage d, (**e**) Stage e. Inversion parameters: max iterations = 8, smoothing factor = 50, damping factor = 100. RMS errors: L2-norm 1.9–2.4%, L1-norm 1.7–2.1%.

L1-norm inversion maintains a linear relationship between true and inverted anomaly sizes, eliminating the jump of independent inversion. The RMS errors of the L1-norm inversion are lower than those of the L2-norm inversion, indicating better convergence with the true model geometry.

We define "time-invariant artifacts" as inversion artifacts that are present in both baseline and monitoring data, caused by factors such as electrode positioning errors, instrument drift, or non-seepage-related near-surface effects. In Figure 5 (L2-norm results), scattered blue and red artifacts appear on the right bank and at depth (x > 30 m, depth > 10 m). These are time-invariant artifacts. In the L1-norm results, these artifacts are effectively suppressed, demonstrating that the L1-norm constraint is more robust against time-invariant artifacts.

These numerical simulations lead to two key conclusions: (1) time-lapse differential inversion is essential for detecting small leakage zones that are invisible in static surveys; (2) L1-norm constraint provides sharper anomaly delineation and better suppression of artifacts compared to L2-norm constraint. Therefore, the L1-norm constrained time-lapse differential inversion is selected as the preferred method for subsequent physical model tests and field applications.

4. Physical Model Test

4.1. Experimental Setup

A physical model test was conducted in an outdoor field to validate the numerical results. The test site was located on a flat farmland area with native clay soil. The fill material used to construct the model dam was collected from the same site and sieved to remove large gravel. The compaction characteristics of the fill soil were determined using the standard Proctor test (ASTM D698 [29]). Air-dried soil samples passing a 5 mm sieve were prepared at different water contents (16% to 32% in 2% increments). Each sample was placed in a 944 cm^3 metal mold in three layers, and each layer was compacted with 25 blows of a 2.5 kg hammer dropping freely from a height of 30 cm. The dry density of each specimen was measured, and a dry density versus water content curve was plotted. The maximum dry density and optimum water content were taken as the peak values of the curve. The measured maximum dry density was 1.52 g/cm^3, and the optimum water content was 24.95%. Figure 6 shows the grain size distribution curve of the fill soil. These values are typical for clayey soils used in embankment construction.

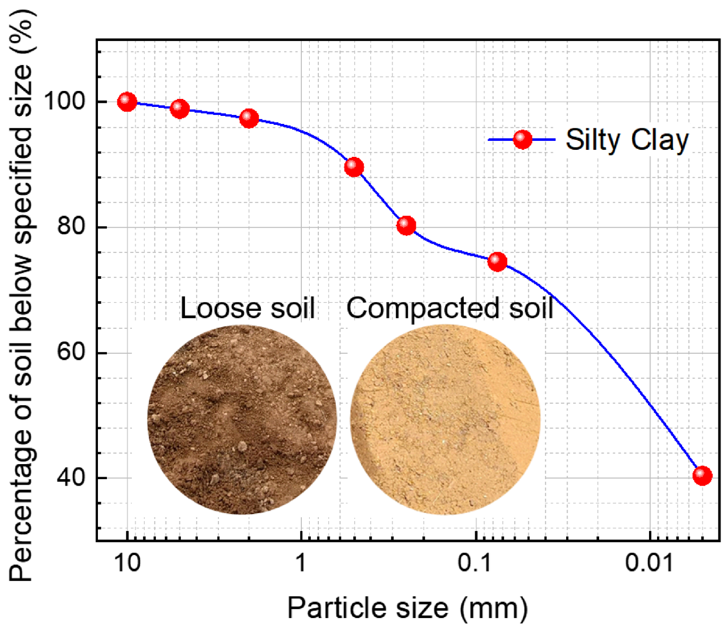

Figure 6. Grain size distribution curve of the fill soil used in the physical model.

The physical dam model had a length of 1.55 m and a height of 0.5 m. The dam foundation was a 0.1 m thick concrete slab. Both abutments were also concrete. The dam body was built by compacting the clay fill in 5-cm lifts, with each lift compacted to achieve a dry density of at least 1.50 g/cm^3. The average water content during compaction was 26.5%, and the final dry density was 1.517 g/cm^3, both satisfying the compaction requirements.

A leakage hazard was intentionally placed in the left abutment. The hazard consisted of a loose, sandy gravel zone (approximately 0.1 m wide and 0.3 m long) that provided a preferential flow path. Three organic glass tubes (piezometers) were installed on a cross-section located 0.85 m from the left dam head to monitor water level changes within the dam body during the experiment. The tubes were placed at three different elevations to capture the phreatic surface.

Complementary laboratory-scale model studies have demonstrated the effectiveness of time-lapse ERT in monitoring water movement through dam filters, confirming the reliability of scaled physical models for seepage detection research [27]. Our model test follows a similar validation strategy to bridge numerical simulations and field applications.

Five monitoring lines were arranged; this paper focuses on line RSL1 on the downstream slope near the left abutment. The starting electrode of this line was placed 0.05 m from the upstream edge of the left dam head. The electrode spacing was 0.05 m, and a total of 32 stainless steel electrodes were inserted into the soil to a depth of 0.03 m to ensure good electrical contact. Data acquisition was performed using a parallel electrical instrument (model: Geopen WBD-1, Geopen Inc., Beijing, China) with a supply voltage of 96 V, a pulse duration of 0.5 s, and a sampling interval of 0.05 s. The AM method (one current electrode, multiple potential electrodes) was used, allowing rapid acquisition (32 readings per injection). Figure 7 shows the experimental setup.

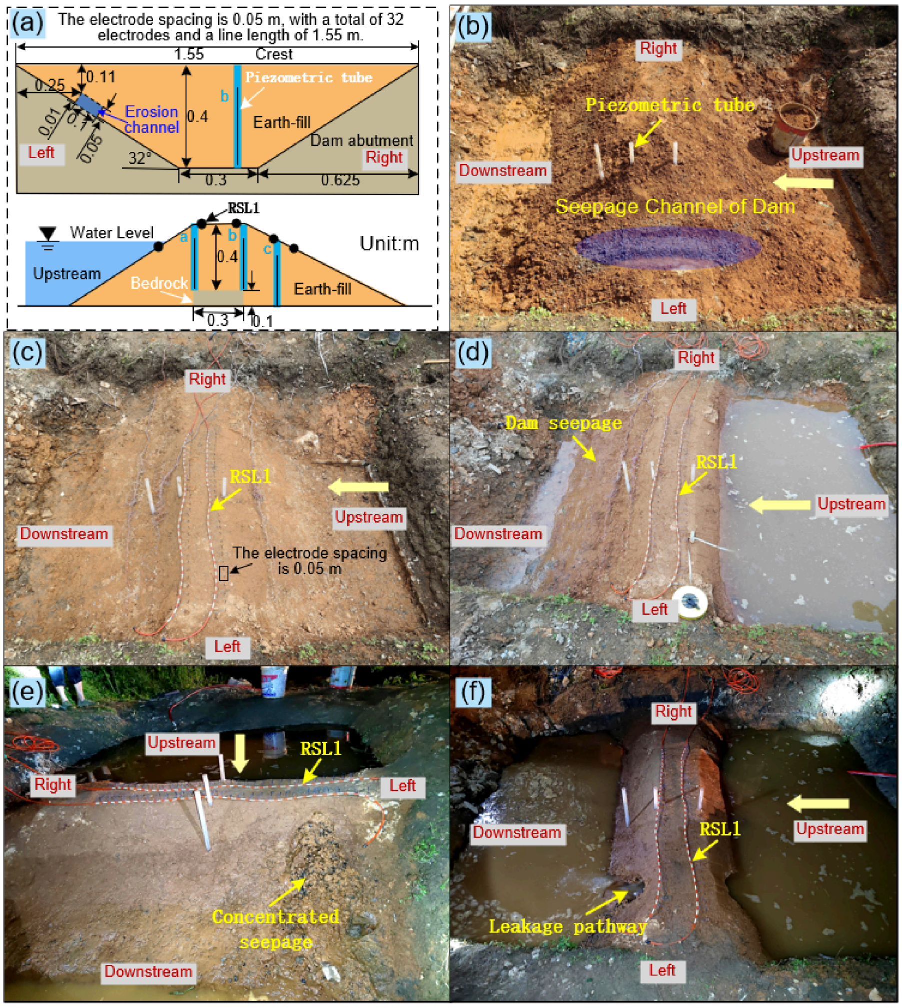

Figure 7. Setup of resistivity monitoring test for seepage at the abutment of an earth dam. (**a**) Overall photo of the model, upstream direction towards left; (**b**) Cross-section showing piezometer placement; (**c**) Detail of electrode installation (spacing 5 cm); (**d**) Electrode line RSL1 on the downstream slope; (**e**) Schematic of the leakage weak-zone location; (**f**) Final state of seepage failure.

4.2. Results

Figure 8 shows the apparent resistivity sections obtained during the physical model test. In the initial dry state (Figure 8a), the left abutment area already exhibits a low-resistivity strip extending diagonally from the upper left to the lower center. This strip corresponds to the leakage hazard—a porous sandy gravel zone retaining moisture. The rest of the dam body shows higher and more uniform resistivity values (approximately 100–200 Ω·m). When the water level rose to 0.06 m below crest (Figure 8b), resistivity decreased. Piezometer readings were 0.27, 0.27, and 0.30 m below crest, showing a nearly horizontal phreatic surface. The low-resistivity strip in the left abutment became wider and more pronounced, suggesting that water was preferentially flowing along the leakage channel. At leakage failure (Figure 8c), resistivity in the left 0.2–0.4 m section dropped below 50 Ω·m, forming a low-resistivity plume, matching the leakage channel geometry. Water seeped from the downstream slope, confirming a through flow path. After a pipe-shaped cavity formed (Figure 8d), overall resistivity remained lower than the dry state, but left abutment resistivity increased slightly from Figure 8c. This is because a water-filled cavity has higher resistivity (~30–100 Ω·m) than saturated soil due to a lack of particles and surface conduction.

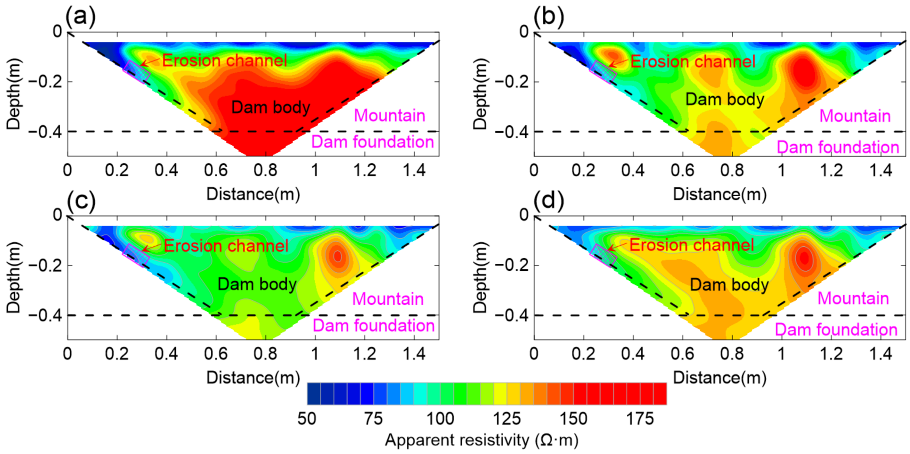

Figure 8. Changes in apparent resistivity of the physical model during the experiment. (**a**) Dry state (no water); (**b**) water level 0.06 m below crest; (**c**) leakage failure at abutment; (**d**) after cavity formation, water levels equalized.

L2-norm inversion (Figure 9a) gives a smooth distribution with isolated high-resistivity closed anomalies at ≈0.1 m depth. These anomalies are likely inversion artifacts (RMS error 12.2%). In contrast, the L1-norm inversion (Figure 9b) yields a more realistic layered structure: resistivity is lower near the surface (around 80–120 Ω·m) and increases gradually with depth (to 150–200 Ω·m at 0.4 m depth). L1-norm regularization produces cleaner, more plausible models (RMS error 10.8%).

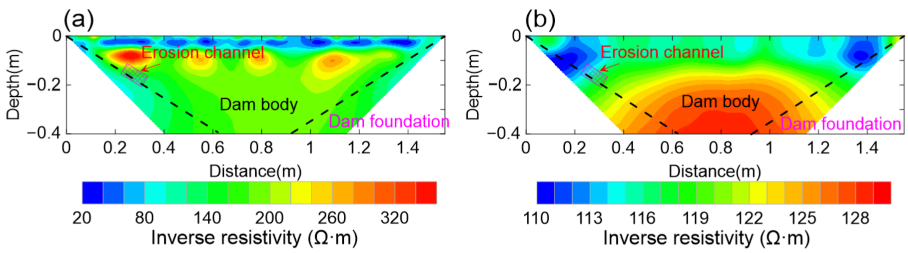

Figure 9. Resistivity inversion profile without reservoir water level. (**a**) L2-norm constraint (RMS 12.2%); (**b**) L1-norm constraint (RMS 10.8%).

Figure 10 shows time-lapse differential inversion results (percentage change) for the four stages with the dry state as the baseline. L2-norm results (left column) show water infiltration decreases resistivity in large parts of the dam. Two main low-resistivity zones are visible: a strong anomaly in the left abutment (the preset leakage channel) and a weaker anomaly near the right side of the dam (0.9–1.1 m from the left edge). The right-side anomaly may be due to a local compaction defect. L2-norm results also show scattered positive changes unrelated to any physical process. RMS errors for L2-norm results: (a) 1.96%, (c) 2.60%, (e) 2.50%.

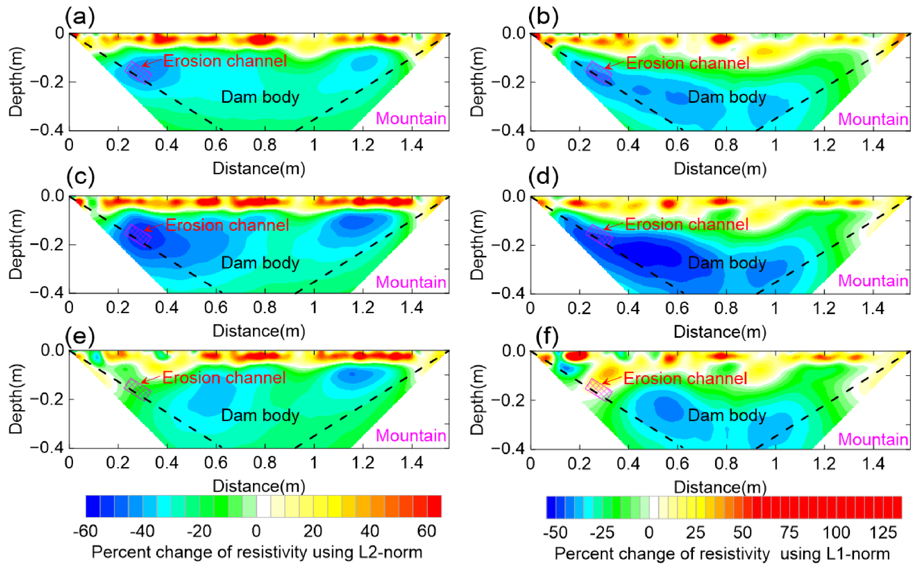

Figure 10. Electrical property changes during the dam seepage failure process obtained by time-lapse differential inversion. Left column (**a**,**c**,**e**): L2-norm constraint; right column (**b**,**d**,**f**): L1-norm constraint. Rows correspond to successive water level stages: (**a**,**b**) Stage b (water level 0.06 m below crest); (**c**,**d**) Stage c (leakage failure at abutment); (**e**,**f**) Stage d (after cavity formation, water levels equalized). Blue indicates resistivity decrease (water saturation), and red indicates increase. In the L2-norm results (**a**,**c**,**e**), the low-resistivity anomaly becomes progressively larger but remains diffuse, with scattered positive artifacts (red) appearing at depth. In contrast, the L1-norm results (**b**,**d**,**f**) show a sharp, well-defined inclined strip of resistivity decrease (40–60%) that expands while preserving a fixed core at the original leakage location. The L1-norm also suppresses the background artifacts seen in the L2-norm results. RMS errors: L2-norm 1.96–2.60%, L1-norm 2.10–2.97%.

L1-norm results (right column) give a sharper image: the left abutment leakage channel is a well-defined inclined strip with a 40–60% resistivity decrease. The boundaries are crisp, matching the visual outflow location. The secondary anomaly on the right is also clearly delineated. As the test progresses from Stage b to Stage c to Stage d, the low-resistivity zone expands in the L1-norm images, but the core of the anomaly (the area of maximum percentage decrease) remains fixed at the location of the original leakage hazard. RMS errors for L1-norm results: (b) 2.10%, (d) 2.61%, (f) 2.97%. Thus, L1-norm time-lapse differential inversion accurately tracks weak-zone evolution while suppressing artifacts.

5. Engineering Case Study

5.1. Site Description and Monitoring Scheme

A clay-core dam located in Zhejiang Province, eastern China, was selected for a field validation of the proposed method. The dam was built in the late 1960s as part of a small irrigation reservoir. The dam crest elevation is 210.5 m above sea level, the crest length is 68 m, and the maximum dam height is 15 m. The upstream slope is protected by riprap, and the downstream slope is grass-covered. The dam foundation consists of weathered granite with varying degrees of fracturing.

A safety assessment conducted in June 2015 revealed persistent leakage from the left abutment. Water was observed seeping from the downstream slope at several locations near the left bank. Although a grouting campaign was carried out to seal the leakage, the problem was not completely solved because the exact location and extent of the leakage pathways were not accurately identified. The grouting was performed based on limited borehole information and experience, leading to incomplete sealing.

On 20 July 2017, a detailed resistivity survey was conducted to map the leakage zone and guide a second round of grouting. Based on the survey results, a targeted grouting operation was performed using a cement–clay mixture (cement:clay ratio 1:2 by weight). After grouting, the visible leakage decreased significantly, but the long-term evolution of the seepage field remained unknown. Therefore, a time-lapse monitoring program was initiated to evaluate the durability of the grouting treatment and to detect any signs of re-activation of leakage.

The present long-term monitoring dataset (2017–2024) builds upon but is distinct from the six surveys reported in Tan et al. (2026) [24]. While Tan et al. focused on electrode array optimization and remote electrode placement, the current paper uses the same field data to evaluate different inversion strategies (independent, ratio, difference) and to compare L1-norm vs. L2-norm constraints. The physical model test and the systematic comparison of L1/L2 norms are entirely new contributions not presented in Tan et al. (2026). Furthermore, an independent geophysical survey by Guo et al. (2022) [25] using self-potential (SP) and ERT on the same dam identified three major seepage paths in the left abutment, which spatially coincide with our high-grout-consumption zones, providing strong multi-method validation.

Monitoring was conducted in 2021, 2022, and 2024. All post-grouting surveys (2021, 2022, 2024) were conducted in late spring to early summer (June–July) under similar climatic conditions (average air temperature 22–25 °C, no rainfall within 72 h prior to each survey). This minimizes seasonal temperature and moisture variations. However, the 2017 baseline survey was conducted in July, also under comparable conditions. Despite this precaution, small inter-annual temperature differences (typically 2–3 °C) and variable antecedent rainfall may still introduce some noise into the resistivity comparisons, as discussed in Section 6. A recent scoping review of climate-resilient flood defenses identified hydro-geophysical imaging, notably time-lapse resistivity, as a key monitoring technology for adapting infrastructure to changing climatic conditions [28]. Our long-term monitoring program directly addresses this need by documenting the multi-year evolution of seepage dynamics under variable reservoir water levels.

Line L1 (Figure 11) was installed on the downstream slope, parallel to the dam axis, at a distance of 0.1 m from the crest measured along the slope. The line started at the left abutment and ended at the right abutment, with a total length of 63 m. Sixty-four stainless steel electrodes were installed at 1 m spacing, each inserted to a depth of 0.15 m to ensure stable contact. The same parallel electrical instrument and AM acquisition mode as in the physical model test were used, with a voltage of 96 V, a pulse duration of 0.5 s, and a sampling interval of 0.05 s. Figure 12 shows photographs of the dam slope at different times. The visible seepage at the toe was substantially reduced after grouting, but some damp patches remained.

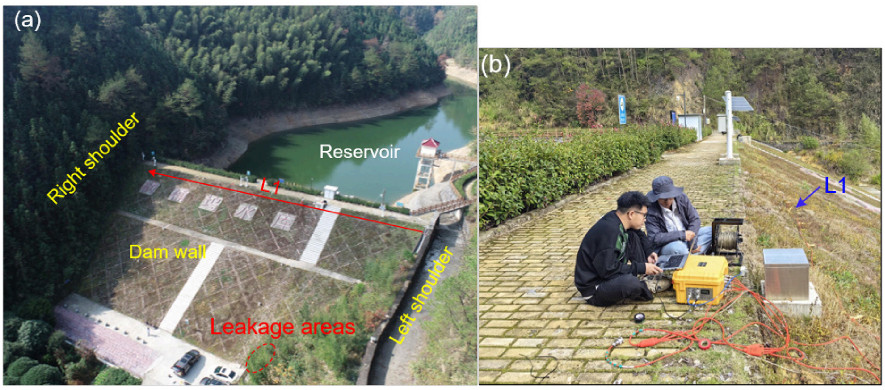

Figure 11. Location of the study area (**a**) and layout of the resistivity monitoring line L1 on the downstream slope (**b**).

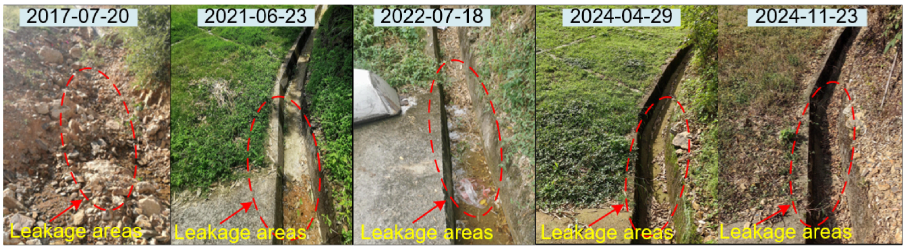

Figure 12. Photographs showing the change in dam slope leakage before and after grouting treatment.

5.2. Evolution of Resistivity After Grouting

Using the data from 20 July 2017 (before grouting) as the baseline, the L1-norm constrained time-lapse differential inversion was applied to the subsequent monitoring datasets. The resistivity percentage change sections are shown in Figure 13. The inversion was performed using the same parameters as in the numerical simulation, with a smoothing factor of 50 and a damping factor of 100, and 8 iterations were sufficient for convergence.

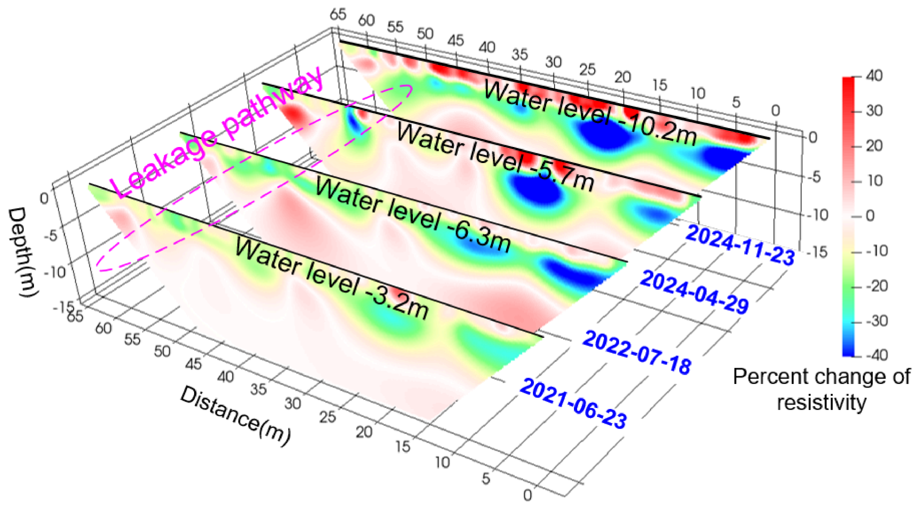

Figure 13. Percentage variation of resistivity at different monitoring stages obtained by L1-norm constrained time-lapse differential inversion.

The results reveal a clear vertical zonation of resistivity change:

Shallow zone (0–2 m depth): The resistivity percentage change is highly variable, with both positive (red) and negative (blue) patches. As the water level decreases (2021–2024), the shallow zone shows increasing resistivity (positive percentage). The high-resistivity patches are discontinuous and irregular. This pattern likely results from surface drying, grass cover, and heterogeneity, not seepage. L1-norm inversion preserves these features without artifacts, but they may not indicate seepage.

Middle zone (2–7 m depth): This zone shows a consistent resistivity decrease of up to 20% across most of the dam length. The decrease is not uniform: two distinct low-resistivity anomalies in the 0–25 m section show 20–55% decreases. These anomalies are present in all post-grouting surveys, although their magnitude changes slightly with reservoir water level. This observation suggests that the grouting material likely filled loose pores, forming a conductive pathway. The cement–clay slurry, with higher water content and ionic concentration than the compacted native fill, produces lower resistivity. Therefore, we interpret these two low-resistivity anomalies as likely indicators of grout-filled zones. This interpretation is further supported by the spatial consistency with the independent SP + ERT survey conducted by Guo et al. [25] on the same dam, which identified three major seepage paths in the left abutment corresponding to these high-grout-consumption areas. The anomalies remain at the same positions in all surveys, showing no new leakage pathways and stable grout over 7 years.

Deep zone (>7 m depth): In contrast to the middle zone, the deep zone shows a resistivity increase of up to 25%. The increase becomes more pronounced as the reservoir water level decreases. This indicates that grouting material solidified poorly coupled rock-soil interfaces. Before grouting, these interfaces were likely saturated with water, giving a low resistivity. After grouting, the cement–clay mixture hardened, reducing the porosity and water content, thereby increasing resistivity. The fact that the deep resistivity increase persists even when the reservoir water level is low (e.g., November 2024, water level 10.2 m below crest) confirms that the grouting created a permanent hydraulic barrier.

The overall pattern of "deep increase, shallow decrease" is therefore a clear signature of successful grouting: the deep pathways have been sealed (resistivity increase), while the shallow injection zone remains conductive due to the presence of the grout itself. The L1-norm time-lapse differential inversion has enabled us to extract this depth-dependent information from the field data, which would be difficult or impossible to obtain from independent inversions of each survey.

The engineering case study demonstrates the practical value of the proposed method. Using the pre-grouting baseline and L1-norm inversion, we: (1) identified two grout-filled zones; (2) evaluated grouting depth (up to 7 m); (3) confirmed 7-year stability; (4) distinguished shallow surface effects from deep hydraulic changes.

6. Discussion

(1) The L1-norm constrained time-lapse difference inversion is significantly superior to L2-norm and independent inversion in anomaly localization and artifact suppression (Figure 5). For the small weak zone at Stage a, independent inversion (Figure 3b, right column) fails to resolve it, whereas L1-norm difference inversion (Figure 5, right column) clearly reveals the anomaly center. The L2-norm results (Figure 5, left column) exhibit scattered background artifacts, which are effectively suppressed by the L1-norm. The RMS errors of the L1-norm inversion are lower than those of the L2-norm, indicating improved convergence. While the sequential difference inversion used in this study has proven effective, recent research has introduced unsupervised data selection strategies for focused time-lapse inversion [23], which can reduce data misfit by clustering data time series and inverting only subsets displaying interesting temporal variations. Future work could integrate this approach to further suppress environmental noise.

(2) Our results are consistent with the blind test at the Røssvatn embankment dam by Sjödahl et al. [30], both demonstrating that time-lapse ERT can effectively locate seepage. However, Sjödahl et al. mainly used independent inversion and ratio images without systematically comparing L1 and L2 norms. The asymmetric time-constraint inversion proposed by Loke et al. [20] shares similarities with our L1-norm difference inversion, but their method focuses on temporal smoothing while ours emphasizes sharp spatial boundaries. In addition, Chambers et al. [15] demonstrated the value of automated time-lapse ERT for groundwater drawdown monitoring. Our study extends these approaches to the specific context of earth-rock dam–abutment leakage, providing a systematic demonstration of the advantage of L1-norm difference inversion for small, growing targets.

Recent advances in dam ERT monitoring have demonstrated the power of geostatistical inversion and multi-source validation. Zhang et al. (2026) [31] used geostatistical ERT to characterize concentrated leakage channels in a full-scale earth dam, achieving fine-scale imaging of channel geometry and water saturation. While their study provides a high-resolution snapshot, our work complements it by capturing the long-term (7-year) dynamic evolution of the resistivity field. Similarly, Liu et al. (2026) [32] proposed an ERT-guided reconstruction framework integrating borehole and GPR data for multi-source validation, which represents a promising direction for reducing interpretation ambiguity. Our single-method long-term monitoring approach, when combined with such multi-source frameworks, could further enhance defect detection reliability.

(3) Several limitations should be acknowledged. First, environmental factors (temperature, rainfall) were not explicitly corrected. Surveys were intentionally scheduled in similar seasons (June–July) to reduce seasonal bias, but inter-annual temperature differences (2–3 °C) and variable antecedent rainfall could still introduce artifacts. A 2 °C increase would cause approximately a 2–4% apparent resistivity decrease, which is smaller than the 20–55% anomalies interpreted as grout-related. Thus, while temperature and rainfall effects cannot be ruled out, they are unlikely to fully explain the observed long-term trends. Second, this study used 2D ERT; real leakage pathways are 3D, and efficient 3D L1-norm inversion algorithms need to be developed. Third, the physical model scale (1.55 m) may affect absolute values, but agreement among numerical, experimental, and field results suggests scale robustness. Fourth, the field case used repeated electrode deployment, introducing repositioning errors; permanently installed electrodes with remote data transmission are the inevitable direction for real-time monitoring. Fifth, the inference that low-resistivity anomalies correspond to grout-filled pathways (Section 5.2) is based solely on geophysical inversion; no direct physical samples were obtained. However, the spatial consistency with the independent SP + ERT survey by Guo et al. (2022) [25] and the temporal correlation with grouting records strengthen this interpretation.

Another critical consideration is the influence of 3D effects caused by heterogeneous embankment conditions. Ball et al. (2026) [33] recently demonstrated through synthetic modeling that off-grid features such as adjoining headponds and concrete abutments can induce 3D effects in 2D ERT inversions, potentially distorting resistivity distributions. While our study acknowledges this limitation, future true 3D ERT surveys using unstructured meshing [34] could mitigate these distortions and improve detection accuracy.

(4) Beyond these limitations, the integration of resistivity monitoring with other geophysical methods (e.g., self-potential, seismic, fiber-optic temperature sensing) could provide complementary information. Multi-physics coupling models would further improve monitoring accuracy. With further development of permanent installation and multi-physics integration, the proposed approach has the potential to become a standard component of dam safety monitoring systems. We recommend the gradual promotion of permanent ERT monitoring systems in important reservoir dams.

7. Conclusions

Through numerical simulation, physical model tests, and a seven-year engineering case study, this work systematically compares different time-lapse resistivity processing methods for earth-rock dam seepage monitoring. The main findings are as follows. First, apparent resistivity and independent inversion are limited by array-dependent distortion, volume effects, and a "sensitivity jump" that delays the detection of small leaks. Ratio-based images improve early detection but retain artifacts. Second, the L1-norm constrained time-lapse difference inversion eliminates this sensitivity jump, provides artifact-free images, and accurately tracks the progressive expansion of the weak zone while preserving the anomaly center at the original leak location. In the physical model test, the L1-norm inversion produced sharper images of the leakage channel and suppressed artifacts compared to L2-norm inversion, with lower RMS errors. Third, post-grouting field monitoring over seven years reveals a layered resistivity signature: deep (>7 m) resistivity increase (up to 25%) due to sealing of rock-soil interfaces, intermediate (2–7 m) decrease (20–55%) marking conductive grout-filled zones, and shallow (0–2 m) scattered changes dominated by environmental factors. This depth-dependent information is only resolvable with time-lapse difference inversion. Fourth, the consistency between our long-term ERT monitoring and the independent SP + ERT survey by Guo et al. (2022) [25] on the same dam reinforces the reliability of the interpreted grout-filled zones and provides a strong basis for dam safety assessment. Overall, the L1-norm time-lapse differential inversion method offers reliable spatiotemporal tracking of leakage hazards and provides practical value for early warning, remediation evaluation, and long-term surveillance without repeated electrode installation. Looking forward, integration of time-lapse ERT with IoT and 5G technologies for automated inversion [16] offers a pathway toward intelligent, real-time dam safety monitoring.

Author Contributions: Conceptualization, L.T.; methodology, L.T.; software, L.T.; validation, L.T., B.S. and P.Z.; formal analysis, L.T.; investigation, L.T.; resources, L.T.; data curation, L.T.; writing—original draft preparation, L.T.; writing—review and editing, B.S. and P.Z.; visualization, L.T. and B.S.; supervision, L.T.; project administration, L.T.; funding acquisition, L.T. All authors have read and agreed to the published version of the manuscript.

Funding: This research was funded by Zhejiang Provincial Natural Science Foundation of China (No. LTGG24D040001), Science and Technology Project of Zhejiang Provincial Department of Water Resources (No. RC2522, No. RC2521), Major Scientific Research Projects of Anhui Higher Education Institutions (No. 2024AH040064), Ministry of Education Anhui Higher Education Research Institute University-Enterprise Joint Talent Cultivation and Key Scientific Research Project (Grant No. JBGS2024GDYJY007), President's Science Foundation Project of Zhejiang Institute of Hydraulics and Estuary (No. ZIHE21Y006, ZIHE23Q014).

Institutional Review Board Statement: Not applicable.

Informed Consent Statement: Not applicable.

Data Availability Statement: This study involves field observation data, numerical simulation data, and theoretical calculation data. The data used to support the findings of this study are available from the corresponding author upon request.

Acknowledgments: The authors have reviewed and edited the output and take full responsibility for the content of this publication.

Conflicts of Interest: Author Lei Tan was employed by the company Zhejiang Guangchuan Engineering Consulting Co., Ltd. The remaining authors declare that the research was conducted in the absence of any commercial or financial relationships that could be construed as a potential conflict of interest. The Zhejiang Guang-chuan Engineering Consulting Co., Ltd. had no role in the design of the study; in the collection, analysis, or interpretation of data; in the writing of the manuscript, or in the decision to publish the results.

References

1. Gao, C.; Hu, J. Impact of climate change on safety of water infrastructures and response measures. *China Water Resour.* **2024**, *24*, 60–67.
2. Li, Z.; Fang, Y.; Lu, Y.; Liu, K.; Zhang, Y. Influences of antecedent rainfall and change of reservoir water level on seepage and stability characteristics of earth rock dams. *Chin. J. Geotech. Eng.* **2022**, *44*, 2177–2186. [CrossRef]
3. Gong, S.; Sun, F.; Huang, W.; Chen, K.; Shen, H. Intelligent monitoring and early warning method for dam safety based on knowledge graph. *Adv. Eng. Sci.* **2024**, *56*, 32–40. [CrossRef]
4. Cai, Y.; Xiang, Y.; Sheng, J.; Meng, Y. Deep-water detection, monitoring, early warning and treatment of emergencies of major water conservancy projects: A review. *Chin. J. Geotech. Eng.* **2023**, *45*, 441–458. [CrossRef]
5. Franco, L.; La Terra, E.; Panetto, L.; Fontes, S. Integrated application of geophysical methods in Earth dam monitoring. *Bull. Eng. Geol. Environ.* **2024**, *83*, 62. [CrossRef]
6. Chen, Y.; Dong, W.; Ren, H.; Li, X. Mise-a-la-masse method, tracer tests and cave detection analysis of underground-river karst-conduit distribution and structure: A case study of the Dafengdong conduits in Guizhou Province, China. *Hydrogeol. J.* **2023**, *31*, 589–600. [CrossRef]

7. Xu, Z.; Yang, Y.; Cao, C. Simulation and analysis of dam leakage inlet detection based on pseudo-flow field method. *J. Appl. Geophys.* **2024**, *228*, 105444. [CrossRef]
8. White, A.; Wilkinson, P.; Boyd, J.; Wookey, J.; Kendall, J.; Binley, A.; Grossey, T.; Chanbers, J. Combined electrical resistivity tomography and ground penetrating radar to map Eurasian badger (Meles meles) burrows in clay-rich flood embankments (levees). *Eng. Geol.* **2023**, *323*, 107198. [CrossRef]
9. Hojat, A.; Arosio, D.; Ivanov, V.; Loke, M.; Longoni, L.; Papini, M.; Tresoldi, G.; Zanzi, L. Quantifying seasonal 3D effects for a permanent electrical resistivity tomography monitoring system along the embankment of an irrigation canal. *Near Surf. Geophys.* **2020**, *18*, 427–443. [CrossRef]
10. Tan, L.; Jiang, X.; Li, H.; Pi, L.; Jiang, S. Application of seepage detection for Jiaowu reservoir dam and directional treatment technology. *Hydropower Energy Sci.* **2019**, *37*, 63–66. [CrossRef]
11. Wilkinson, P.; Uhlemann, S.; Chambers, J.; Meldrum, P.; Loke, M. Development and testing of displacement inversion to track electrode movements on 3-D electrical resistivity tomography monitoring grids. *Geophys. J. Int.* **2015**, *200*, 1566–1581. [CrossRef]
12. Martinho, E. Electrical resistivity and induced polarization methods for environmental investigations: An overview. *Water Air Soil Pollut.* **2023**, *234*, 215. [CrossRef]
13. Ball, J.; Chambers, J.; Wilkinson, P.; Binley, A. Resistivity imaging of river embankments: 3D effects due to varying water levels in tidal rivers. *Near Surf. Geophys.* **2023**, *21*, 93–110. [CrossRef]
14. Tresoldi, G.; Arosio, D.; Hojat, A.; Longoni, L.; Zanzi, L. Long-term hydrogeophysical monitoring of the internal conditions of river levees. *Eng. Geol.* **2019**, *259*, 105139. [CrossRef]
15. Chambers, J.; Meldrum, P.; Wilkinson, P.B.; Ward, W.; Jackson, C.; Matthews, B.; Joel, P.; Kuras, O.; Bai, L.; Uhlemann, S.; et al. Spatial monitoring of groundwater drawdown and rebound associated with quarry dewatering using automated time-lapse electrical resistivity tomography and distribution guided clustering. *Eng. Geol.* **2015**, *193*, 412–420. [CrossRef]
16. Cai, Z.; Yang, M.; Wang, J.; Xu, Y. Dynamic monitoring of earth-rock dam body leakage based on time-lapse electrical resistivity method. *Comput. Tech. Geophys. Geochem. Explor.* **2026**, *48*, 244–252. [CrossRef]
17. Lu, J.; Wang, B.; Li, D.; Duan, J. Application of mine resistivity method monitoring system in water hazard prevention of coal mining face. *Coal Geol. Explor.* **2022**, *50*, 36–44. [CrossRef]
18. LaBrecque, D.; Yang, X. Difference inversion of ERT data: A fast inversion method for 3-D in situ monitoring. *J. Environ. Eng. Geophys.* **2001**, *6*, 83–89. [CrossRef]
19. Perri, M.; Cassiani, G.; Gervasio, I.; Deiana, R.; Binley, A. A saline tracer test monitored via both surface and cross-borehole electrical resistivity tomography: Comparison of time-lapse results. *J. Appl. Geophys.* **2012**, *79*, 6–16. [CrossRef]
20. Loke, M.; Wilkinson, P.; Chambers, J.; Uhlemann, S.; Dijkstra, T.; Dahlin, T. The use of asymmetric time constraints in 4-D ERT inversion. *J. Appl. Geophys.* **2022**, *197*, 104536. [CrossRef]
21. Tao, T.; Han, P.; Ma, H.; Tan, H. 3-D inversion of time-lapse resistivity data. *Chin. J. Geophys.* **2024**, *67*, 3973–3988. [CrossRef]
22. Loke, M.; Acworth, L.; Dahlin, T. A comparison of smooth and blocky inversion methods in 2D electrical imaging surveys. *Explor. Geophys.* **2003**, *34*, 182–187. [CrossRef]
23. Hermans, T.; Maene, A.; Caudron, C.; Vanhooren, L. Unsupervised data selection for focused time-lapse inversion in electrical resistivity tomography monitoring. *Geophysics* **2026**, *91*, A19–A23. [CrossRef]
24. Tan, L.; Zhang, P.; Xu, H.; Jiang, X.; Hu, X.; Liang, D.; Zhang, Y. Long-term monitoring of embankment dam seepage evolution using time-lapse electrical resistivity tomography. *J. Appl. Geophys.* **2026**, *251*, 106313. [CrossRef]
25. Guo, Y.; Cui, Y.; Xie, J.; Luo, Y.; Zhang, P.; Liu, H.; Liu, J. Seepage detection in earth-filled dam from self-potential and electrical resistivity tomography. *Eng. Geol.* **2022**, *306*, 106750. [CrossRef]
26. Miller, C.; Routh, P.; Brosten, T.; McNamara, J. Application of time-lapse ERT imaging to watershed characterization. *Geophysics* **2008**, *73*, G7–G17. [CrossRef]
27. Hojat, A.; Ferrario, M.; Arosio, D.; Brunero, M.; Ivanov, V.; Longoni, L.; Madaschi, A.; Papini, M.; Tresoldi, G.; Zanzi, L. Laboratory Studies Using Electrical Resistivity Tomography and Fiber Optic Techniques to Detect Seepage Zones in River Embankments. *Geosciences* **2021**, *11*, 69. [CrossRef]
28. Eze, K.; Kehinde, T.; Anosike, C.; Dirisu, C.; Turoti, K.; Oparinde, A. Geotechnical approaches to climate-resilient flood defenses: A scoping review of design, monitoring, and risk management. *Discov. Civ. Eng.* **2026**, *3*, 99. [CrossRef]
29. *ASTM D698*; Standard Test Methods for Laboratory Compaction Characteristics of Soil Using Standard Effort (12,400 ft-lbf/ft^3 (600 kN-m/m^3)). ASTM: West Conshohocken, PA, USA, 2019.
30. Sjödahl, P.; Dahlin, T.; Johansson, S. Using the resistivity method for leakage detection in a blind test at the Røssvatn embankment dam test facility in Norway. *Bull. Eng. Geol. Environ.* **2010**, *69*, 643–658. [CrossRef]
31. Zhang, B.; Liang, Y.; Wang, P.; Dai, L.; Yeh, T.; Zhang, H.; Xu, B.; Yin, C.; Xia, R.; Sun, Z. Characterizing concentrated leakage channels in full-scale earth dam using geostatistical electrical resistivity tomography: An on-site case study. *J. Hydrol.* **2026**, *666*, 134756. [CrossRef]

32. Liu, X.; Liu, S.; Jia, Z.; Tan, C.; Vogt, D.; Tian, S.; Zhao, Q.; Liu, X.; Lu, Q. ERT-guided reconstruction of defect patterns in earth-filled dams with multi-source validation. *Eng. Geol.* **2026**, *369*, 108788. [CrossRef]
33. Ball, J.; Butler, K.; Chambers, J.; Wilkinson, P.; Binley, A. Implications of heterogeneous embankment conditions for geoelectrical investigations on dams: A case study at Mactaquac Dam, Canada. *Near Surf. Geophys.* **2026**, *Early View*. [CrossRef]
34. Chen, X.; Tan, L.; Yang, X.; Wu, X.; Zhou, G.; Zhang, Q. Three-dimensional electrical resistivity tomography for earth-rock dam seepage detection: Integrating real-world topography, water levels and unstructured meshing. *Near Surf. Geophys.* **2025**, *23*, 572–584. [CrossRef]

https://doi.org/10.3390/app16115654